PNAS RESEARCH ARTICLE | MICROBIOLOGY OPEN ACCESS

SRS-FISH: A high-throughput platform linking microbiome metabolism to identity at the single-cell level

Xiaowei Ge[a,1], Fátima C. Pereira[b,1], Matthias Mitteregger[b,2], David Berry[b], Meng Zhang[a], Bela Hausmann[c,d], Jing Zhang[e], Arno Schintlmeister[b], Michael Wagner[b,f,3], and Ji-Xin Cheng[a,e,3]

Edited by Dianne Newman, California Institute of Technology, Pasadena, CA; received February 28, 2022; accepted April 8, 2022

One of the biggest challenges in microbiome research in environmental and medical samples is to better understand functional properties of microbial community members at a single-cell level. Single-cell isotope probing has become a key tool for this purpose, but the current detection methods for determination of isotope incorporation into single cells do not allow high-throughput analyses. Here, we report on the development of an imaging-based approach termed stimulated Raman scattering–two-photon fluorescence in situ hybridization (SRS-FISH) for high-throughput metabolism and identity analyses of microbial communities with single-cell resolution. SRS-FISH offers an imaging speed of 10 to 100 ms per cell, which is two to three orders of magnitude faster than achievable by state-of-the-art methods. Using this technique, we delineated metabolic responses of 30,000 individual cells to various mucosal sugars in the human gut microbiome via incorporation of deuterium from heavy water as an activity marker. Application of SRS-FISH to investigate the utilization of host-derived nutrients by two major human gut microbiome taxa revealed that response to mucosal sugars tends to be dominated by Bacteroidales, with an unexpected finding that Clostridia can outperform Bacteroidales at foraging fucose. With high sensitivity and speed, SRS-FISH will enable researchers to probe the fine-scale temporal, spatial, and individual activity patterns of microbial cells in complex communities with unprecedented detail.

chemical imaging | multimodal microscopy | microbiome heterogeneity | mucus degradation | single-cell microbiology

Significance

Microbial communities play fundamental roles in the functioning of environmental and human-associated ecosystems. Yet, conventional experimental approaches to study the function of individual microbes in their native habitat are highly time consuming, allowing analysis of only a few cells or samples. Here, we report the development of a high-throughput stimulated Raman scattering–two-photon fluorescence in situ hybridization (SRS-FISH) platform to investigate the metabolism and identity of uncultivated microorganisms with single cell–level resolution. SRS-FISH enabled us to detect metabolic responses of over 30,000 cells from human gut microbiome taxa to mucosal sugars. Metabolism and identity analysis of multiple samples revealed that microbiome response to mucosal sugars is individual specific and that Clostridia may have been overlooked as mucosal sugar degraders.

With the rapid advances in both genotyping and phenotyping of single cells, bridging genotype and phenotype at the single-cell level is becoming a new frontier of science (1). Methods have been developed to shed light on the genotype–metabolism relationship of individual cells in a complex environment (2, 3), which is especially relevant for an in-depth understanding of complex microbial communities in the environment and host-associated microbiomes. For functional analyses of microbial communities, single-cell isotope probing is often performed in combination with nanoscale secondary ion mass spectrometry (NanoSIMS) (4–7), microautoradiography (MAR) (8, 9), or spontaneous Raman microspectroscopy (10–12) to visualize and quantify the incorporation of isotopes from labeled substrates. These methods can be combined with fluorescence in situ hybridization (FISH) using ribosomal ribonucleic acid (rRNA)-targeted probes (13), enabling a direct link between metabolism and identity of the organisms. In addition, Raman-activated cell sorting has been recently developed using either optical tweezers or cell ejection for downstream sequencing of the sorted cells (14–16). While these approaches have expanded the possibilities for functional analyses of microbiome members (17), all of the aforementioned methods suffer from extremely limited throughput. Consequently, only relatively few samples and cells per sample are typically analyzed in single-cell stable isotope probing studies, hampering a comprehensive understanding of the function of microbes in their natural environment.

To overcome the limited throughput of Raman spectroscopy, coherent Raman scattering microscopy based on coherent anti-Stokes Raman scattering (CARS) or stimulated Raman scattering (SRS) has been developed (18, 19). Compared with CARS, the SRS signal is free of the electronic resonance response (20) and is linear to molecular concentration, thus permitting quantitative mapping of biomolecules (21, 22). Both CARS and SRS microscopy have successfully been applied for studying single-cell metabolism in eukaryotes (23–26). In a label-free manner, SRS imaging has led to the discovery of an aberrant cholesteryl ester storage in aggressive cancers (27, 28), lipid-rich protrusions in cancer cells under starvation (29), and fatty acid unsaturation in ovarian cancer stem cells (30) and more recently, in melanoma (31, 32). CARS and SRS have also been harnessed to explore lipid metabolism in live *Caenorhabditis elegans* (33–36). Combined with stable isotope probing, SRS microscopy has allowed the tracing of glucose metabolism in

The authors declare no competing interest.

This article is a PNAS Direct Submission.

[1]X.G. and F.C.P. contributed equally to this work.

[2]Present address: The Wallenberg Laboratory, Department of Molecular and Clinical Medicine, Sahlgrenska Academy, University of Gothenburg, 41345 Gothenburg, Sweden.

[3]To whom correspondence may be addressed. Email: michael.wagner@univie.ac.at or jxcheng@bu.edu.

This article contains supporting information online at https://www.pnas.org/lookup/suppl/doi:10.1073/pnas.2203519119/-/DCSupplemental.

Published June 21, 2022.

eukaryotic cells (37, 38) and the visualization of metabolic dynamics in living animals (25). Recently, SRS was successfully applied to infer antibiotic resistance patterns of bacterial pure cultures and heavy water (D_2O) metabolism (39). Yet, SRS microscopy has not been adapted for studying functional properties of members of microbiomes as SRS itself lacks the capability of identifying cells in a complex community.

Here, we present an integrative platform that exploits the advantages of SRS for single-cell stable isotope probing together with two-photon FISH for the identification of cells in a high-throughput manner. To deal with the challenges in detecting low concentrations of metabolites inside small cells with diameters around 1 μm, we have developed a protocol that maximizes the isotope label content in cells and exploits the intense SRS signal from the Raman band used for isotope detection.

Conventionally, FISH is performed separately by one-photon excited fluorescence microscopy (40). To enhance efficiency, we developed a system that implements highly sensitive SRS metabolic imaging with two-photon FISH using the same laser source. These efforts collectively led to a high-throughput platform that enables correlative imaging of cell identity and metabolism at a speed of 10 to 100 ms per cell. In comparison, it takes about 20 s to record a Raman spectrum from a single cell in a conventional spontaneous Raman FISH experiment (41, 42).

Our technology enabled high-throughput analysis of single-cell metabolism in the human gut microbiome. In the human body, microbes have been shown to modulate the host's health (43, 44). Analytical techniques looking into their activities and specific physiologies (i.e., phenotype) as a result of both genotype and the environment provide key information on how microbes function, interact with, and shape their host. As a proof of principle, we used stimulated Raman scattering–two-photon fluorescence in situ hybridization (SRS-FISH) to track the incorporation of deuterium (D) from D_2O into a mixture of two distinct gut microbiota taxa. Incorporation of D from D_2O into newly synthesized cellular components of active cells, such as lipids and proteins, occurs analogously to incorporation of hydrogen from water during the reductive steps of biosynthesis of various cellular molecules (10, 45, 46). Importantly, D incorporation from D_2O has been shown to be reliable to track metabolic activity of individual cells within complex microbial communities in response to the addition of external substrates (10, 17, 47). When microbial communities are incubated in the presence of D_2O under nutrient-limiting conditions, individual cells display only minimal activity and only minor D incorporation (11, 17, 47). In contrary, when cells are stimulated by the addition of an external nutrient, cells that can metabolize this compound become active and incorporate D into macromolecules, which lead to the presence of C-D bonds into the cell's biomass. Consequently, D incorporation from D_2O can be combined with techniques able to detect C-D signals, such as Raman-based approaches, and to track metabolic activity at the single-cell level in response to a variety of compounds. Here, we show that SRS-FISH enables fast and sensitive determination of the D content of individual cells while simultaneously unveiling their phylogenetic identity. We applied this technique to complex microbial communities by tracking in situ the metabolic responses of two major phylogenetic groups of microbes in the human gut (Bacteroidales and Clostridia spp.) and of a particular species within each group to supplemented host-derived nutrients. Our study revealed that 1) Clostridia spp. can actually outperform Bacteroidales spp. at foraging on the mucosal sugar fucose and shows 2) a significant interindividual variability of responses of these major microbiome taxa toward mucosal sugars. Together, our results demonstrate the capability of SRS-FISH to unveil the metabolism of particular microbes in complex communities at a throughput that is two to three orders of magnitude higher than other metabolism identity bridging tools, therefore providing a valuable multimodal platform to the field of single-cell analysis.

Results

An SRS-FISH Platform to Link Cell Metabolism with Cell Identity. SRS can visualize chemical information by coherently probing Raman active vibrations with two synchronized pulsed pump and Stokes beams. When the energy difference is tuned to the vibrational energy of the targeted chemical bond, a chemical concentration map can be generated. In our case, considering that C-H and C-D stretching vibrations are spectrally broad, we used femtosecond pulses to maximize the detection sensitivity (48). The use of femtosecond pulses facilitates efficient two-photon excited FISH on the same SRS microscope. The SRS and FISH signals are sequentially detected in the forward direction using a photodiode and two silicon photomultipliers, respectively. The energy schematic and the setup are shown in Fig. 1 *A* and *B*. Details can be found in *Materials and Methods*.

To retrieve information on the activity of single bacterial cells in pure culture or in complex samples, live cells present in simple (pure cultures) or complex (gut microbiome) samples were incubated in D_2O-containing media (10, 39) to enable incorporation of D into biomolecules of metabolically active cells (Fig. 1*C*). Cells need to be metabolically active but not necessarily growing to incorporate D, as synthesis of new biomolecules already leads to D incorporation (10). Cells were subsequently fixed and subjected to FISH using fluorescently labeled oligonucleotide probes targeting rRNA in order to reveal their phylogenetic identity (Fig. 1 *C* and *D*). Samples prepared in this way were consecutively imaged to retrieve 1) fluorescence signals from hybridized samples and 2) chemical information that enables determination of cellular D enrichment levels for the different taxa targeted by FISH (Fig. 1*D*).

We have developed a two-photon FISH protocol to detect cyanine 3 (Cy3) and cyanine 5 (Cy5), two dyes that possess large two-photon cross-sections (49) and are commonly used in FISH studies due to their brightness. Two silicon photomultipliers were used to selectively detect the fluorescence emitted by Cy3 and Cy5 (Fig. 1*D*). We confirmed that two-photon excited fluorescence (TPEF) retrieves accurate fluorescence information with comparable imaging quality and speed as achieved by a confocal microscope (further discussed below). Thus, two-photon FISH is a reliable tool for identity mapping, although with slightly lower spatial resolution (~300 nm) than confocal microscopy (usually ~200 nm) (*SI Appendix*, Fig. S1).

To determine D incorporation into bacteria, the pump and Stokes beams were tuned to target the C-D vibrational peak (2,168 cm^{-1}). As bacterial cells have sizes that are comparable with the laser focus laterally and axially (*SI Appendix*, Fig. S1), the different volumes exhibited by different bacterial species can influence the SRS intensity level. To compensate for this effect, the pump beam was tuned to target the center of the C-H bond vibrational peak (2,946 cm^{-1}) as a reference signal for intensity normalization. In terms of absolute concentrations, measurements of dimethyl sulfoxide (DMSO)/H_2O mixtures revealed that as low as around 3 million C-D bonds or C-H bonds can reliably be detected by femtosecond SRS within the excitation volume. We have observed that some bacterial species generated signals in the silent spectral regions (from 1,800 to 2,800 cm^{-1}) that can be detected by SRS but not by spontaneous Raman spectroscopy (*SI Appendix*, Fig. S3), which

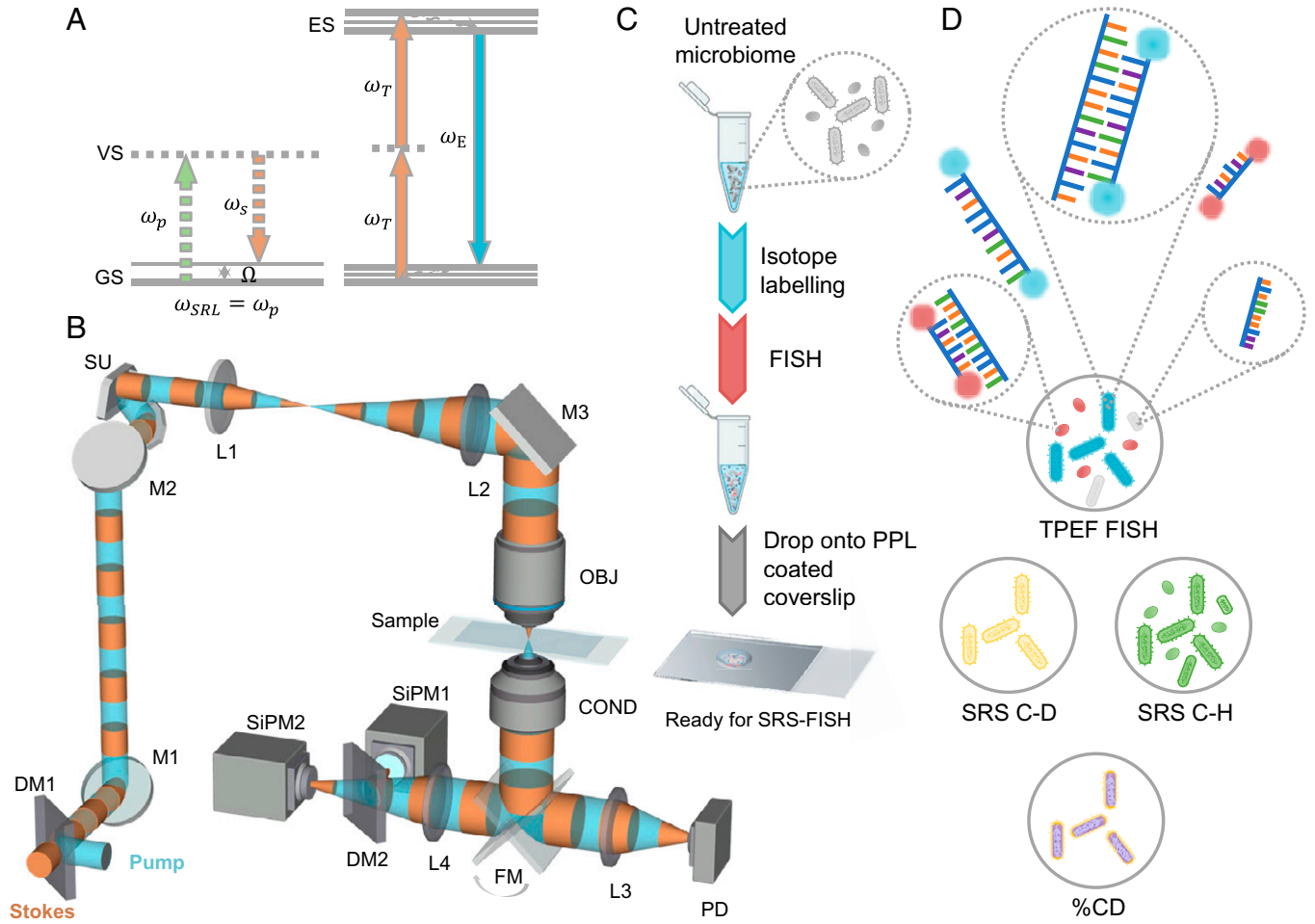

Fig. 1. SRS-FISH platform to link phylogenetic identity (genotype) with metabolic activity (phenotype) of microbes. (*A*) SRS and TPEF mechanism. ES, excited state; GS, ground state; VS, virtual state; Ω, vibrational energy; ω_E, fluorescence emission frequency; ω_P, pump beam laser frequency; ω_S, Stokes beam laser frequency; ω_{SRL}, stimulated Raman loss frequency; ω_T, TPEF excitation beam frequency. (*B*) SRS-FISH instrumental setup. M1 to M3 are mirrors. DM1 and DM2 are dichroic mirrors. L1 to L4 are lenses. SiPM1 and SiPM2 are silicon photomultipliers. COND, condenser; FM, flip mirror; OBJ, objective; PD, photodiode; SU, scanning unit. (*C*) Typical sample procedure process for SRS-FISH experiments. Pure bacterial cultures or complex microbiome samples are incubated in D_2O-containing media to enable D incorporation into metabolically active cells. Samples are subsequently fixed and subjected to FISH. After FISH, samples are deposited in a glass cover slide and analyzed by SRS-FISH. (*D*) Schematic representation of SRS-FISH imaging results. Samples are hybridized with fluorescently labeled oligonucleotide probes (double labeled with either cyan or red fluorophores) targeting taxa of interest present in the sample. Fluorescence signal originating from hybridized samples (cyan and red) is then overlaid with the SRS C-D signal (yellow) and the SRS C-H signal (green) to reveal metabolic activity levels represented by %CD (magma) of each identified bacterial cell. Organisms not targeted by the probes will not display fluorescence (gray).

may originate from other nonlinear processes, such as transient absorption, photothermal lensing, and cross-phase modulation (50, 51). In order to correct this unspecific background, off-resonance images were recorded with the pump beam tuned to target 2,479 cm^{-1} in the silent region and subtracted from both C-D and C-H SRS images (*SI Appendix*, Figs. S3 and S4). Via combination of the individual signal intensities, a quantity can be defined that expresses the metabolic activity in D incorporation as $\%CD_{SRS}$, calculated from the SRS signal intensities at C-D, C-H, and off resonance, according to the formula $\%CD_{SRS} = (I_{CD} - I_{off})/(I_{CD} + I_{CH} - 2I_{off})$, where I stands for intensity (Fig. 1*D* and *Materials and Methods*).

SRS Has Sufficient Sensitivity to Detect Single Metabolically Active Bacteria Tagged by FISH. Although SRS has been used before (but without combining it with FISH) for imaging isotope incorporation in bacterial and mammalian cells (25, 39), a more comprehensive study about D isotope labeling detected by SRS imaging on different bacterial species has not been conducted yet. In order to evaluate the optimum measurement settings, a first trial with two cultures of *Escherichia coli* cells grown in M9 mineral (M9) medium, one without the addition of D_2O (natural isotope abundance control) and the other one after addition of heavy water (50% D_2O), was performed. For each culture, 81 image scans, conducted with 10 µs per pixel dwell time, were recorded within randomly selected fields of view (FOVs). Analysis of these datasets revealed that 10 scans, corresponding to a measurement time of around 1 ms per single cell (*SI Appendix*, Fig. S2), are sufficient for obtaining adequate precision in the determination of %CD values under maintenance of the high throughput of the technique (*SI Appendix*, *SI Text*).

To further investigate the suitability of SRS-FISH to detect the incorporation of D in cells with different physiologies and cell wall structures, we performed SRS measurements on four bacterial cultures that have been hybridized with fluorescently labeled probes (FISH): *Bacteroides thetaiotaomicron* (gram negative) (Fig. 2*A*), *Clostridium scindens* (gram positive) (Fig. 2*B*), *E. coli* (gram negative) (Fig. 2*C*), and *Blautia producta* (gram positive) (Fig. 2*D*). These cultures were grown in rich (brain heart infusion [BHI] or Luria–Bertani [LB]), semiminimal (Bacteroides minimal medium supplemented with aminoacids [BMMs]), or minimal (Bacteroides minimal medium [BMM] or M9) media

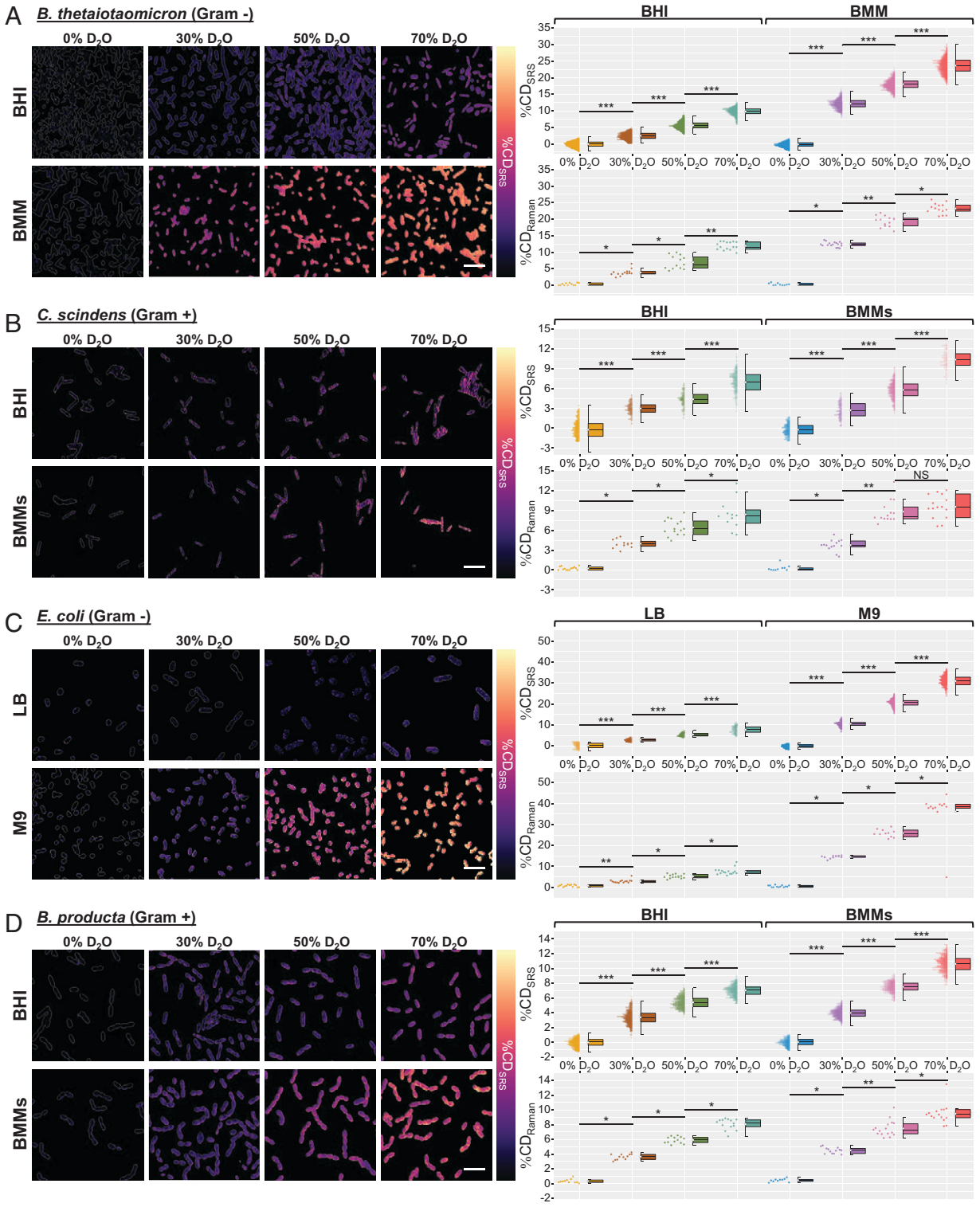

Fig. 2. Sensitivity of the SRS-FISH platform to detect D_2O metabolic incorporation into bacterial cells hybridized with fluorescently labeled rRNA-targeted oligonucleotide probes. SRS imaging and single-cell statistics on %CD by SRS and spontaneous Raman of (*A*) *B. thetaiotaomicron* cells grown in BHI or BMM media, (*B*) *C. scindens* cells grown in BHI or BMMs media, (*C*) *E. coli* cells grown in LB or M9 media, and (*D*) *B. producta* cells grown in BHI or BMMs media containing increasing concentrations of D_2O. Cell contours are indicated by gray lines. $\%CD_{SRS}$ scaling: (*A*) minimum 0, maximum 30%; (*B*) minimum 0, maximum 20%; (*C*) minimum 0, maximum 40%; and (*D*) minimum 0, maximum 20%. Per pixel dwell time: 100 μs. Details regarding data processing are in *SI Appendix*, Fig. S4. The combined dot and box plots in *Right* refer to the single-cell %CD values measured with either SRS or spontaneous Raman spectroscopy. Each dot represents a cell. Boxes represent medians and first and third quartiles. Whiskers extend to the highest and lowest values that are within one and a half times the interquartile range. The white circles in the centers of the boxes indicate the mean values of the data distribution. Please note that the negative $\%CD_{SRS}$ values originate from off-resonance background correction. NS, nonsignificant, $P > 0.05$. * $10^{-5} < P < 0.05$ (two-sided Mann–Whitney *U* test); ** $10^{-7} < P < 10^{-5}$ (two-sided Mann–Whitney *U* test); *** $P < 10^{-7}$ (two-sided Mann–Whitney *U* test). (Scale bars, 5 μm.)

containing various concentrations of D_2O and therefore, covering a wide range of cellular D contents (Fig. 2). The lowest mean D labeling content ($\%CD_{SRS}$) that could be detected in single cells grown under all the above conditions was around 2.4% (*B. thetaiotaomicron* cultured in BHI medium with 30% D_2O), which still showed statistical significance against the negative

control (two-sided Mann–Whitney U test, $P < 10^{-10}$), cultured in the same medium but in the absence of D_2O. In addition, a linear relationship between the cellular $\%CD_{SRS}$ values and the D_2O concentration in the applied media was observed. A few exceptions occurred at 70% D_2O (Fig. 2 *B* and *D*), which can be explained by the inhibitory effect exerted by elevated concentrations of heavy water on metabolic activity. As expected from previously published data (52), cells grown in complex-rich media or semiminimal media displayed lower levels of D incorporation compared with cells grown in minimal media containing equivalent concentrations of heavy water (Fig. 2). This is likely caused by the higher need for de novo biosynthesis of monomeric biomolecules (which will become labeled during synthesis), such as amino acids, nucleotides, or fatty acids, which are absent in minimal media but readily available in unlabeled form for direct uptake and incorporation from complex (or semiminimal) media.

We further studied the impact of FISH on the D enrichment level measured by SRS. Both cell fixation and FISH protocols have been previously shown to elute material (e.g., lipids) from microbial cells, which can impact the D content as assessed by spontaneous Raman (4, 10, 42). Using SRS-FISH, we could observe a relative decrease by $13.65\% \pm 7.81\%$ in the C-D level of *E. coli* hybridized cells (FISH) compared with fixed but nonhybridized *E. coli* cells (no FISH; $P < 0.05$, Mann–Whitney U test) (*SI Appendix*, Fig. S5) for both media tested. This reduction in %CD is approximately three times smaller than reported for a similar comparison performed with spontaneous Raman measurements (10) and might be explained by the fact that in the FISH protocol used here, the exposure time of the cells to ethanol was reduced compared with the previously applied protocol (*Materials and Methods*). Therefore, our optimized FISH protocol causes a comparatively small loss in cellular biomass and thus minimizes the impact single of FISH on cell metabolic activity analyses.

Overall, SRS microscopy enabled efficient detection and discrimination of both gram-positive and gram-negative hybridized cells displaying a wide range of D content, with mean $\%CD_{SRS}$ values ranging from as low as 2.4% up to 30% (Fig. 2 *A* and *C*) ($P < 0.05$, two-sided Mann–Whitney U test). To validate the accuracy of femtosecond SRS for detection of bacterial activity, we compared $\%CD_{SRS}$ with %CD values measured by spontaneous Raman microspectroscopy ($\%CD_{Raman}$) (10). Under our conditions, SRS displayed similar sensitivity as spontaneous Raman (Fig. 2). However, SRS analysis is two to three orders of magnitude faster than achieved with spontaneous Raman (10 to 100 ms per cell vs. 20 s per cell) (42). This high speed enables SRS measurements of a much larger number of cells, therefore increasing the power of statistical analysis and throughput. It is challenging to quantitatively compare the %CD value distribution patterns of SRS and spontaneous Raman due to the difference in the measurement principle (*SI Appendix*, *SI Text*). However, the data from our pure culture experiments clearly revealed that SRS-FISH is a fast and versatile platform to track metabolic activity in FISH-targeted bacteria.

SRS Is Compatible with Two-Photon FISH to Link Microbial Metabolism with Identity. As both SRS and TPEF are multiphoton processes, the compatibility of these two schemes requires further validation. Cellular contents labeled with fluorescent dyes can lead to background signals detected by SRS, impacting the $\%CD_{SRS}$ values. This can occur when a fluorophore absorbs one photon from the pump and one photon from the Stokes beam. The simultaneous absorption of photons from the two distinct beams could interfere with the SRS signal through a phenomenon known as nondegenerate two-photon absorption. Although two-photon absorption can be calculated based on the absorption cross-sections of the utilized dyes, there are scant data of nondegenerate two-photon absorption to estimate its influence on SRS. In our setup, we could not detect any interference on SRS attributable to the fluorophores in the sample, as we did not observe any significant differences in the %CDs values of hybridized compared with nonhybridized cells grown in the absence of D_2O for the two different media tested (*SI Appendix*, Fig. S5) (0% D_2O). Therefore, the lower %CDs values obtained after FISH in D-labeled cells are not caused by an interference with the dyes used for FISH with SRS imaging (*SI Appendix*, Fig. S5).

We then evaluated the compatibility of using the pump beam at 852 nm and the Stokes beam at 1,045 nm to excite the Cy3 and Cy5 dyes attached to the FISH probes (Fig. 3*A*). The two

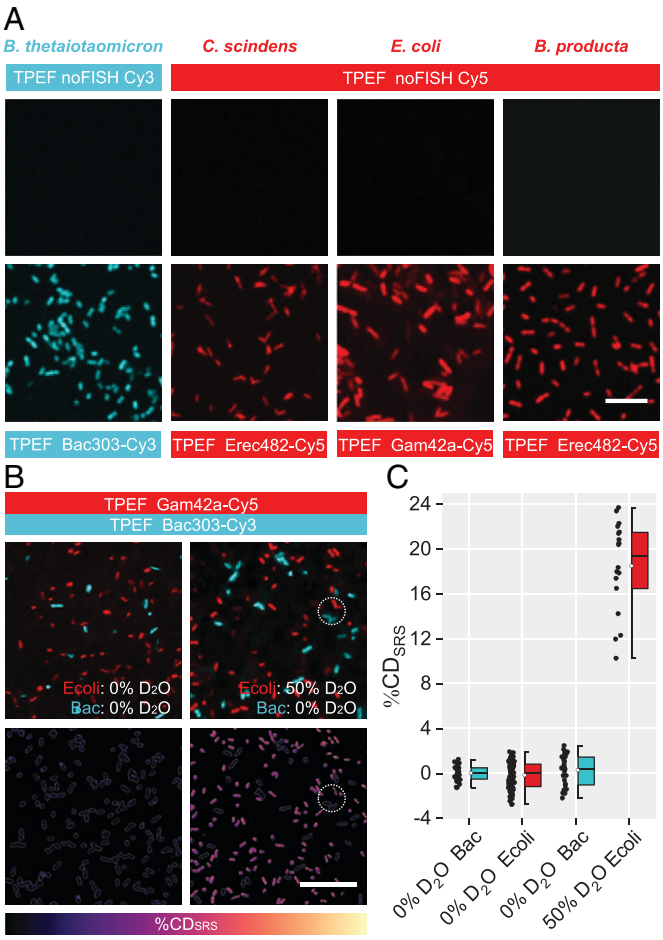

Fig. 3. Phylogenetic and phenotypic information can be acquired simultaneously by the SRS-FISH platform without interference. (*A*) TPEF visualization of D-labeled *B. thetaiotaomicron*, *C. scindens*, *E. coli*, and *B. producta* cells hybridized (FISH) with Bac303-Cy3 (pseudocolored cyan), Erec482-Cy5 (pseudocolored red), or Gam42a-Cy5 (pseudocolored red) oligonucleotide probes or not (noFISH). No background in TPEF channels is detected for D-labeled nonhybridized cells. Imaging was performed under dry conditions. (Scale bar, 10 μm.) (*B*) Simultaneous SRS and TPEF imaging of artificial mixtures of unlabeled (0% D_2O) *B. thetaiotaomicron* and *E. coli* cells (*Left*) or of D-labeled (50% D_2O) *E. coli* and unlabeled (0% D_2O) *B. thetaiotaomicron* cells (*Right*) cultured in minimal media. $\%CD_{SRS}$ values are shown for both mixtures. In both cases, cells were hybridized with the taxa-specific probes Bac303-Cy3 (cyan) and Gam42a-Cy5 (red), enabling cells from the two populations to be distinguished by TPEF imaging. In *Lower*, cell contours are shown with gray lines. The dashed circles highlight the different D content of the two taxa. $\%CD_{SRS}$ scaling: minimum 0, maximum 60%. Bac, *B. thetaiotaomicron*; Ecoli, *E. coli*. (Scale bar, 15 μm.) (*C*) Single-cell $\%CD_{SRS}$ value distribution in the two different populations of the artificial mixtures presented in *B*. Please note that the negative $\%CD_{SRS}$ values originate from off-resonance background correction.

silicon photomultipliers sensitively detected the emission from D-labeled *B. thetaiotaomicron* cells hybridized with a Bac303-Cy3 oligonucleotide probe and of D-labeled *C. scindens*, *E. coli*, and *B. producta* cells hybridized with an Erec482-Cy5 or Gam42a-Cy5 oligonucleotide probe (Fig. 3*A* and *SI Appendix*, Table S1) (53, 54). For particular biological samples, it has been shown that the femtosecond beams used for SRS may generate signals in the visible range and therefore, interfere with TPEF imaging (55). However, only a negligible TPEF signal was detected from bacterial cells that were not hybridized (Fig. 3*A*), and therefore, we conclude that SRS does not interfere with TPEF in our application.

Having confirmed that SRS and two-photon FISH are compatible, we applied SRS-FISH to an artificial mixture of *E. coli* and *B. thetaiotaomicron* cells, each hybridized with taxa-specific oligonucleotide probes labeled with a different dye (Fig. 3*B*). As a first approach, both *E. coli* and *B. thetaiotaomicron* cells were grown in minimal medium without the addition of D_2O. Under these conditions, both cell populations displayed close to zero levels of D incorporation (Fig. 3 *B*, *Left*). When we analyzed a mixture of D-labeled *E. coli* and non–D-labeled *B. thetaiotaomicron* cells, D incorporation was observed from *E. coli* cells targeted with the Gam42a-Cy5 probe, while *B. thetaiotaomicron* targeted by the Bac303-Cy3 probe displayed no D labeling (Fig. 3 *B*, *Right*, highlighted circles). Using the signal obtained from TPEF, masks were generated by CellProfiler (*Materials and Methods*) for either of the FISH-targeted populations (*SI Appendix*, Fig. S4), enabling automated $\%CD_{SRS}$ calculation for each FISH-targeted population. While Cy5-tagged *E. coli* cells displayed %CD values of around 20, which reflected D incorporation from the D_2O in the M9 medium, Cy3-tagged *B. thetaiotaomicron* cells displayed %CD values close to 0, as expected (Fig. 3*C*).

High-Throughput SRS-FISH for Identifying Mucosal Sugar Utilizers in the Human Gut Microbiome. To demonstrate the applicability of the SRS-FISH setup to identify active taxa within a complex microbial community, we examined the responses of specific taxa from the human gut microbiota to additions of sugars contained in the mucus layer (56, 57) (Fig. 4*A*). Gut commensals able to forage on mucin play a pivotal role in resistance to pathogen colonization and in modulating the host immune response (56, 57). In previous work, D_2O combined with spontaneous Raman-activated cell sorting revealed that members of the families Muribaculaceae, Bacteroidaceae, and Lachnospiraceae are major mucosal sugar foragers in the mouse gut, and whole-genome sequencing revealed that the vast majority of these organisms indeed have genomic potential to catabolize these sugars (17). However, given the differences in microbiota composition of mice and humans as well as differences in predominant types of mucus glycans that can be found in the two hosts (58, 59), it remains to be clarified if the same taxa are efficient mucosal sugar utilizers in the human gut and what their substrate preferences are. For this purpose, freshly collected human fecal samples were incubated with the five different mucin *O*-glycan sugars (*N*-acetylneuraminic acid [NeuAc], *N*-acetylglucosamine [GlcNAc], *N*-acetylgalactosamine [GalNAc], fucose, and galactose) in M9 minimal medium (without glucose) containing 50% D_2O (Fig. 4*A*). In this work, we chose M9 medium because it is a defined minimal medium where the only carbon source is the sugar amended, so one can expect very low metabolic activity in the absence of the substrate of interest (*SI Appendix*, *SI Text*). Under these conditions, we observed that human gut microbes responded to the amended mucosal sugars as well as to glucose (used as a positive control) by incorporating D into their biomass, as revealed using spontaneous Raman (Fig. 4*B*). As expected, only negligible incorporation of D was detected for cells that had been incubated in the presence of D_2O but in the absence of any amended sugar, reflecting very low metabolic activity driven, for example, by storage products or substrates released from decaying bacteria (Fig. 4*B*).

Next, we proceeded to identify which taxa respond to specific sugars in fecal samples from three different volunteers using the SRS-FISH platform. Note that the human experiments were conducted with informed consent and approved by the University of Vienna Ethics Committee (reference no. 00161). For this purpose, oligonucleotide probes targeting two of the most dominant and widespread phylogenetic groups of microbes in the human gut (60, 61) were applied: Bac303-Cy3 targeting *Bacteroides* and *Prevotella* (53) among other Bacteroidales and Erec482-Cy5 targeting members of the family Lachnospiraceae (also denominated *Clostridium* clusters XIVa and XIVb) (62) (*SI Appendix*, Table S1). Additionally, we selected these probes because a large percentage of organisms identified as efficient mucosal sugar foragers in the mouse and human gut are targeted or are closely related to organisms targeted by these probes (17, 63), and a large proportion of Bacteroidales spp. and Clostridia spp. have been shown to carry genes for mucosal sugar catabolism (63). High-throughput amplicon sequencing of the 16S rRNA gene of microbiome samples included in our study revealed that Bac303-targeted organisms belonged mostly to the *Bacteroides*, *Prevotella_9*, and *Parabacteroides* genera within the phylum Bacteroidota (Fig. 2 *C* and *D*), which was the most abundant phylum in all samples. Organisms covered by the Erec-482 probe largely belonged to several Lachnospiraceae genera as well as to the genus *Roseburia*, the *Ruminococcus torques* group, and the *Eubacterium eligens* group within the phylum Firmicutes (Fig. 4 *C* and *D*). Interestingly, microbiome samples clustered by volunteer ($P < 0.001$, $r^2 = 0.85$, permutational multivariate analysis of variance) (Fig. 4*E*) rather than by supplementation of mucosal sugar, indicating that the short incubation time and conditions employed prevented major shifts in community composition due to the amended sugar. Nevertheless, amplicon sequencing revealed some fluctuations in relative abundances of taxa targeted by both the Bac303 and Erec482 probes in response to the different mucosal sugars amended (Fig. 4 *F* and *G*). Fractions of Bac303- and Erec482-targeted taxa determined by amplicon sequencing differed from fractions determined by imaging of FISH-labeled cells under dry conditions (Fig. 4 *F* and *G*, *Discussion*, and *Materials and Methods*), which can be attributed to different biases and limitations of either method (64, 65). Despite this, shifts in fractions of both taxa in response to sugars detected by FISH correlated well with shifts detected by amplicon sequencing (Fig. 4 *F* and *G*), therefore indicating that the TPEF FISH approach is sensitive to capture the microbiome response to mucosal sugar amendment.

A challenge encountered in imaging of the complex gut microbiome samples by SRS-FISH was that the TPEF signal from fluorescently labeled cells bleached much faster than observed with pure cultures. To overcome this limitation, we acquired the TPEF signals from microbiome samples in a dried state to slow down bleaching while maintaining FISH imaging accuracy (*SI Appendix*, Figs. S6 and S7). Subsequently, the samples were immersed by the addition of water for maintaining the SRS intensity and sensitivity achieved in a liquid environment (*SI Appendix*, Fig. S6 and *SI Text*). Using the SRS-FISH protocol optimized for complex microbiome samples, we examined the response of cells targeted by the Bac303-Cy3 and Erec482-Cy5 probes to each mucosal sugar in fecal samples from three different

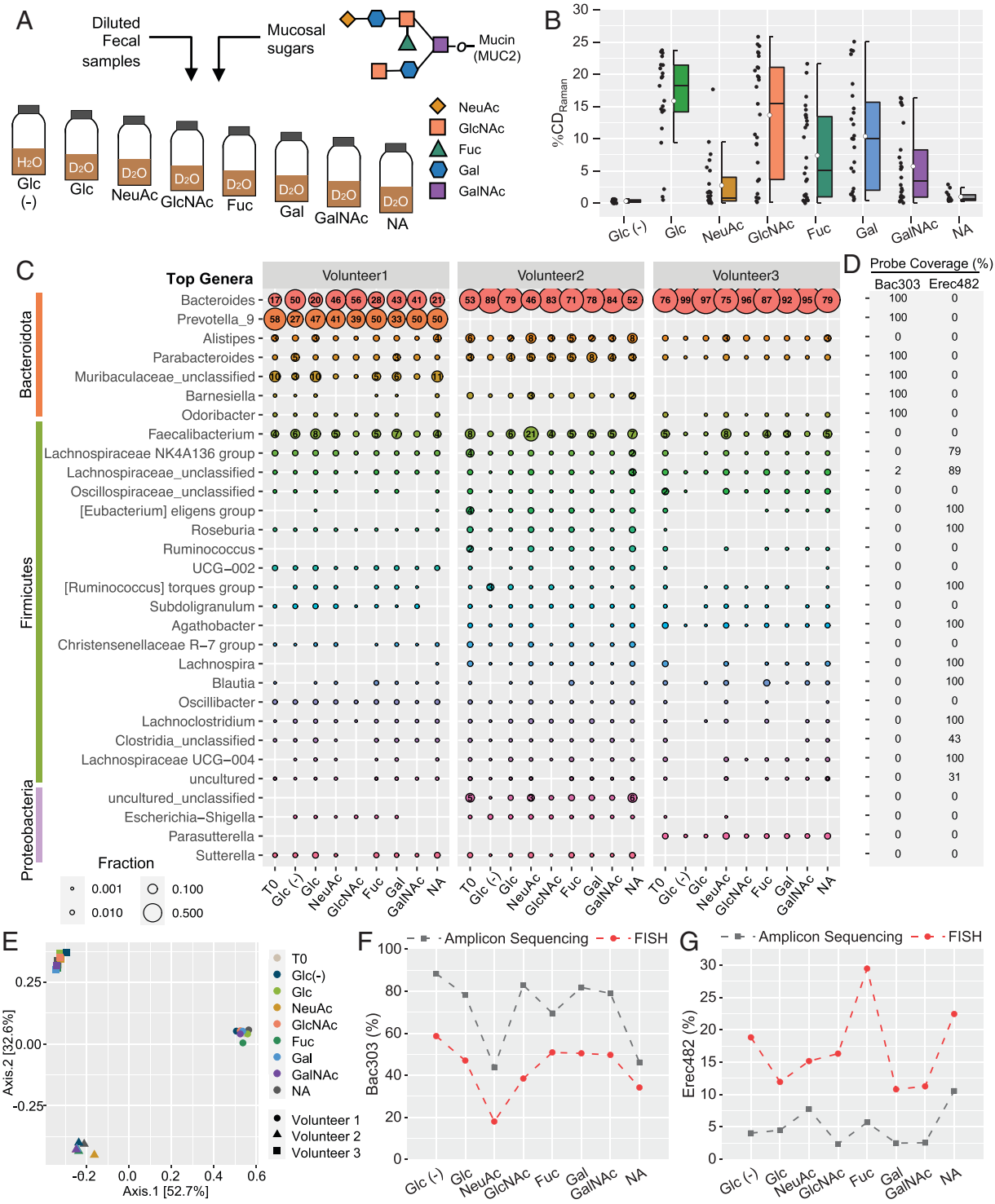

Fig. 4. Utilization of mucosal sugars by the gut microbiome. (*A*) Illustration of the experimental setup. Freshly collected human fecal samples were diluted in minimal M9 medium and supplemented with different mucus *O*-glycan sugars in the presence of 50% D_2O under anaerobic conditions. Negative and positive control incubations were performed in parallel by incubating the samples with glucose (Glc) in the presence of H_2O [labeled Glc (–)] or D_2O (labeled Glc). Mucus *O*-glycan sugars include NeuAc, GlcNAc, fucose (Fuc), galactose (Gal), and GalNAc. A no amendment (NA) control with D_2O but no sugar added was also included. Cells from all microcosms were hybridized with FISH probes and subsequently probed for D incorporation using spontaneous Raman or D incorporation into taxa of interest using SRS-FISH. (*B*) D content of randomly selected microbiome members supplemented with the different mucosal sugars and controls as described in *A* measured by spontaneous Raman microspectroscopy. Each dot represents a cell. Boxes represent medians and first and third quartiles. Whiskers extend to the highest and lowest values that are within one and a half times the interquartile range. The white circles in the centers of the boxes indicate the mean values of the data distribution. (*C*) Bubble plot representing the relative abundances of the top 30 genera detected across all microbiome samples as determined by 16S rRNA gene amplicon sequencing after correcting for the different copy numbers of the 16S rRNA gene across different taxa. The respective phylum for each represented genus is indicated on the left. Labels tagging all samples for which relative abundances are $>$ 2% ($>$ 0.02 fraction) are shown. T0 denotes a sample collected immediately after incubation setup. (*D*) Coverage of the Bac303 and Erec482 FISH probes for each of the indicated genera. (*E*) Compositional variation between samples (principal coordinates analysis based on Bray–Curtis dissimilarities) colored according to the sugar supplemented for the three microbiome volunteers indicated by different shapes. (*F* and *G*) Fractions of the microbiome community that either match the probe sequence (as determined by 16S rRNA amplicon sequencing and BLASTN (nucleotide basic local alignment search tool) analysis) or display labeling (as assessed by counting FISH-labeled cells imaged by TPEF) for the Bac303 probe (*F*) and the Erec482 probe (*G*) in incubations of microbiome samples from volunteer 2.

volunteers (Fig. 5 and *SI Appendix*, Fig. S8). The response to mucosal sugars differed from volunteer to volunteer (one-way ANOVA test, $P < 2.225 \times 10^{-308}$) (*SI Appendix*, Fig. S9) both in quantitative and qualitative terms. Quantitatively, the overall microbiome response to the amended sugars (with respect to the number of active cells and their %CD values) was the highest for volunteer 2, while the lowest cellular activity was detected for volunteer 3 (*SI Appendix*, Figs. S9 and S10). This is not surprising given that the human microbiome is highly individualized and also, that different fecal samples have been reported to contain different fractions of viable cells (66, 67). For volunteers 1 and 2, between 95 and 100% of the analyzed cells became active and isotopically labeled in response to glucose, which emphasizes that the incubation conditions applied

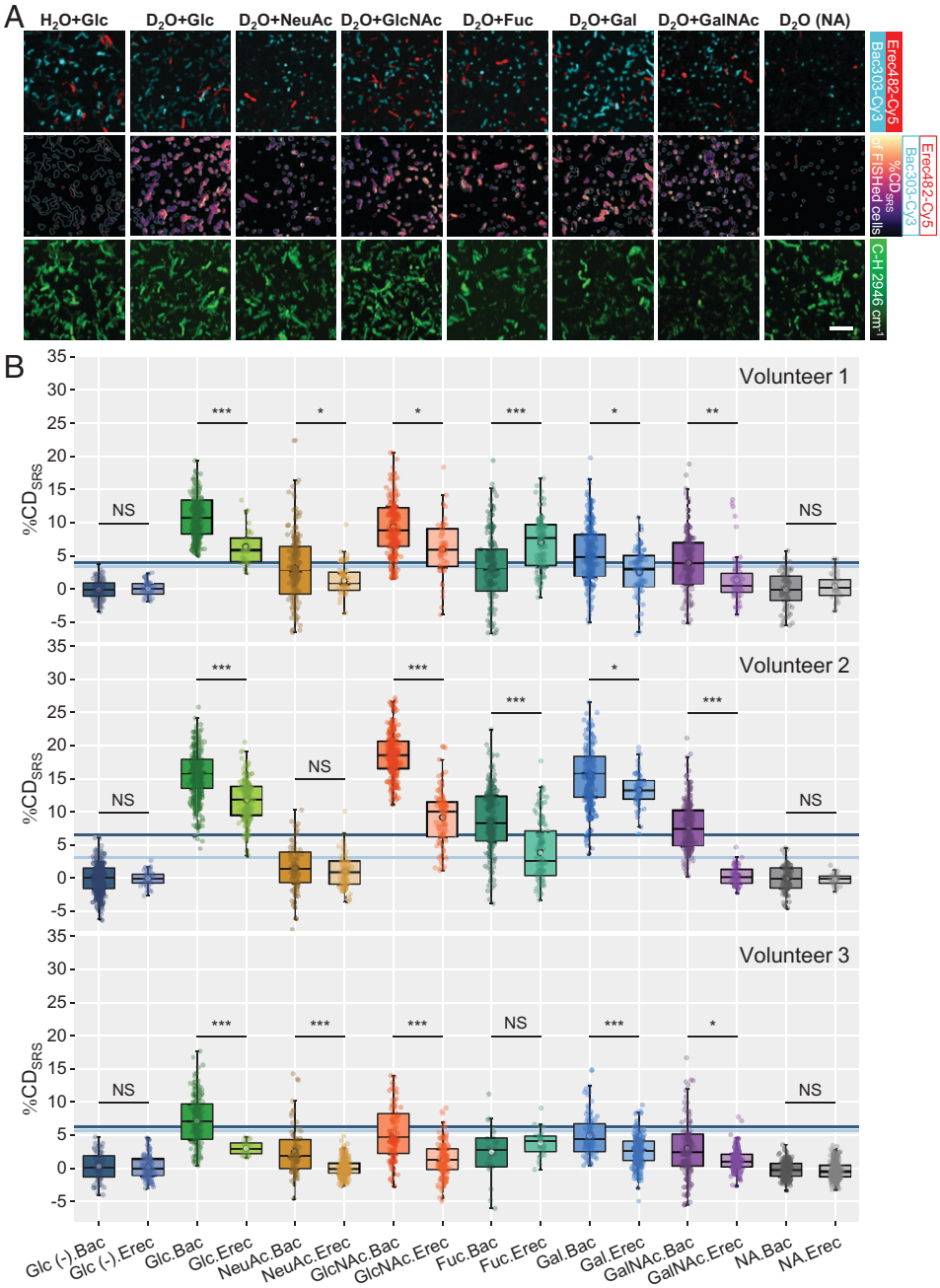

Fig. 5. SRS-FISH uncovers the ability of major gut microbiome taxa to forage on different mucosal sugars. (*A*) Microbiome samples of volunteer 1 were incubated with different mucosal sugars and hybridized with the oligonucleotide probes Bac303-Cy3 (cyan) and Erec482-Cy5 (red). Representative images obtained by TPEF (*Top*) and SRS (%CD_{SRS} with FISH contours are in *Middle*, %CD_{SRS} values of other microbes are not displayed to enhance clarity, and C-H in log scale displaying all microbes is in *Bottom*) are shown. %CD_{SRS} scaling: minimum 0, maximum 25%. In *Middle*, cells with FISH tag are shown with respective color contour lines. Negative control: H_2O + glucose. Positive control: D_2O + glucose. Details regarding data processing are in *SI Appendix*, Fig. S4. NA, no amendment. (Scale bar, 10 μm.) (*B*) Single-cell C-D level distribution in the two different targeted taxa presented in *A* measured by SRS for samples from three different volunteers. Box plots represent the median and first and third quartiles, with the extended lines representing the minimum and maximum values within 1.5 interquartile ranges from the first and third quartiles. The white circles in the centers of the boxes indicate the mean values of the data distribution. The deeper gray blue line (mean + 3 SD of Bac303-Cy3–labeled cells in negative control samples) indicates the threshold value for consideration of Bac (Bac303-Cy3) cells as significantly D enriched. The lighter gray blue line (mean + 3 SD of Erec482-Cy5–labeled cells in negative control samples) indicates the threshold value for consideration of Erec482-Cy5 (Erec) cells as significantly D enriched (refer to *SI Appendix*, Fig. S10). The two-sided Mann–Whitney *U* test was applied to compare the statistical significance between Bac and Erec bacteria for each amendment. Please note that the negative %CD_{SRS} values originate from off-resonance background correction. NS, nonsignificant, $P > 0.05$. * $10^{-5} < P < 0.05$; ** $10^{-7} < P < 10^{-5}$; *** $P < 10^{-7}$.

in this study enable potentially all microbiome members to respond and get D labeled (*SI Appendix*, Figs. S9 and S10). Across the three samples, the highest average number of active cells (and higher %CD values) was recorded in response to the mucosal sugar GlcNAc followed by the response to galactose (*SI Appendix*, Figs. S9 and S10), which is in agreement with the results obtained by spontaneous Raman (Fig. 4*B*). Overall, we could detect a significant response of both FISH-targeted taxa to the mucosal sugars in all the samples analyzed, with the exception of Erec482-targeted taxa to GalNAc in the sample from volunteer 1 (Fig. 5*B* and *SI Appendix*, Table S2). In none of the samples did the no amendment control lead to the stimulation of a significant number of cells (Fig. 5*B* and *SI Appendix*, Table S2). Furthermore, the response of Bac303-targeted taxa was overall higher than the response from Erec482-targeted taxa across all volunteers for all supplemented sugars with the exception of fucose, where the inverse was observed for two of the volunteers (Fig. 5 and *SI Appendix*, Fig. S10). These findings hold even by taking into consideration that the unspecific signals in the C-D region were higher in the control group (H_2O) for Bac303-targeted cells than for Erec482-targeted cells (Fig. 5). We further extended the SRS-FISH analysis by applying FISH probes targeting particular species within Bacteroidales [*Bacteroides vulgatus*, targeted by the Bvulg1017-Cy3 probe (60)] and Lachnospiraceae [*Agathobacter rectalis*, formerly *Eubacterium rectale*, targeted by the Erec996 + Erec1252-Cy5 probe (68)] that have been previously proposed either to contribute to mucin degradation (*B. vulgatus*) (69) or to preferentially associate with the mucin layer (*A. rectalis*) (70) (*SI Appendix*, Fig. S11 and Table S1). For volunteer 2, we observed that the response from *A. rectalis* was low for all mucosal sugars tested, suggesting that it may be a poor mucus degrader despite its ability to colonize the mucus layer (*SI Appendix*, Fig. S11). Importantly, this analysis also revealed that *B. vulgatus* is one of the most efficient sialic acid consumers within Bacteroidales, with Bvulg1017-targeted cells overall displaying higher levels of metabolic activity in response to this sugar when compared with cells targeted by the broader Bac303 probe (Fig. 5 and *SI Appendix*, Fig. S11*B*).

Discussion

Microbial communities are fundamental to the functioning of all ecosystems and the health of animals, plants, and humans. These microbiomes are typically investigated by metaomic analyses that generate valuable annotation-based hypotheses regarding the metabolism of their members but are not suited for testing these hypotheses as gene annotations are often missing, wrong, or incomplete (71). Furthermore, many microbes have cell cycles and show considerable phenotypic diversity within isogenic strains, and the activity of microbes is influenced by their spatial arrangement in their habitat. Thus, there is an urgent need for direct functional analyses of microbes within complex samples with single-cell resolution.

SRS-FISH fills a gap among the available tools linking metabolism and identity in complex microbial communities due to its exceptionally high throughput (10 to 100 ms per cell). Overall, SRS-FISH is at least two orders of magnitude faster than state-of-the-art methods: MAR FISH (2 to 20 d per sample) (72), Raman-activated microbial cell sorting (>7.22 s per cell) (14), FISH NanoSIMS [>10 s per cell (73), which does not include the long preconditioning time], and spontaneous Raman FISH (~20 s per cell) (42). Furthermore, implementation of FISH by TPEF can be advantageous when imaging thick biological specimens or live organisms, as near-infrared excitation enables deeper penetration into biological samples and causes less damage to cells (40).

The application of SRS-FISH to the gut microbiome demonstrated the suitability of our approach to link identity to metabolism within complex microbial communities and at the same time, revealed interesting findings related to mucosal sugar foraging in the human gut. SRS-FISH measurements showed that Bacteroidales spp. tend to dominate the response to mucosal sugars over Clostridia spp. in all of the tested individuals (Fig. 5 and *SI Appendix*, Fig. S10). Indeed, the notion that *Bacteroides* spp. are major mucus degraders has been demonstrated by several studies (17, 63, 74). However, our results revealed that organisms from the *Clostridium* clusters XIVa/XIVb also substantially contribute to mucosal sugar degradation. Further, we show that larger fractions of Clostridia cells can forage on fucose compared with Bacteroidales cells (Fig. 5 and *SI Appendix*, Fig. S10). Fucose is an important sugar in the colon as it occupies a terminal position on host glycans, thus being at the interface of microbiota–mucus interactions (75). About 20% of human individuals naturally lack a functional copy of the *FUT2* gene and thus, lack almost all gut fucosylation (76). Genome-wide association studies have shown that these individuals have an increased susceptibility to inflammatory diseases linked to the gut microbiota, such as Crohn's disease (77, 78). Additionally, mice that lack the Fut2 enzyme have simpler gut microbiomes that are accompanied by a decrease in unclassified Clostridiales (78). These findings, together with our results, suggest that Clostridia may have been overlooked as fucose degraders in the gut (56). Elucidating which particular Erec482-targeted organisms use fucose may be key to designing individualized probiotic interventions aiming to restore the homeostasis in humans lacking *FUT2*, therefore reducing their predisposition to gastrointestinal disease.

Another interesting finding from our study is that the pattern of mucosal sugar foraging differs between the murine and human microbiome; human gut bacteria preferentially metabolize GlcNAc (Fig. 5 and *SI Appendix*, Fig. S9), while the preferred sugar of the murine microbiome is galactose (17). This could reflect the different overall compositions of human and murine colonic mucins (i.e., while the human colonic mucin carries predominantly GlcNAc-containing core 3– and core 4–based *O*-glycans, the murine colonic mucin is mostly characterized by galactose-containing core 1– and core 2–type structures) (58, 59). This finding may have important implications when translating results from mouse studies into humans.

There are several opportunities to further improve our SRS-FISH platform. These improvements include SRS-selective scanning of FISH-targeted cells, which can even further improve the throughput of SRS-FISH when the taxa of interest appear in very low abundance. Also, laser equipment with upgraded wavelength tuning speed will also provide the potential to gain higher throughput (79). Other than the throughput, the sensitivity and resolution of SRS-FISH can also be improved by implementing visible SRS (80, 81). Of note, the excitation beam in visible SRS can efficiently excite fluorophores from cells targeted by FISH and help avoid the TPEF bleaching issue when imaging cells in a liquid environment. On the other hand, the number of taxa simultaneously tracked by SRS-FISH can be substantially increased using spectral unmixing and custom-designed FISH probes (82–84). Regarding metabolism probing, besides using D_2O as an activity marker to induce C-H peak shifts, D-labeled substrates and other stable isotopes, such as ^{13}C and ^{15}N, could be used to track the metabolism of particular compounds and provide information on major catabolic activities and pathways. By targeting spectral features between 400 and 1,800 cm^{-1} (16),

SRS could fingerprint major intracellular macromolecules that display shifts upon incorporation of stable isotopes. This could potentially be achieved by the implementation of hyperspectral SRS with ultrafast delay-line tuning and machine learning into the SRS-FISH platform (85). SRS-FISH would also be a useful tool to probe the distribution of several storage compounds and intrinsic biomolecules in diverse eukaryotic and prokaryotic cells (86–89).

In summary, we have developed an exceptionally high-throughput SRS-FISH platform and successfully applied this tool to identify efficient mucosal sugar utilizers in the human gut microbiome. SRS-FISH can be applied to a broad range of environmental samples (e.g., marine sediments, soil), including those where some autofluorescence background is an issue because SRS is more resilient to sample autofluorescence than spontaneous Raman (20, 90). Meanwhile, SRS-FISH is not limited to microbiome samples. With the state-of-the-art SRS metabolism imaging and versatile FISH techniques, such as probing abnormal proliferation of chromosomes or targeting messenger ribonucleic acid (mRNA), SRS-FISH will be broadly applicable to eukaryotes. By allowing the scanning of multiple samples in a fast and sensitive manner, SRS-FISH is well suited to reveal fine-scale temporal, individual, and spatial patterns in a variety of specimens, which can otherwise be missed by existing methods due to their low throughput.

Materials and Methods

SRS-FISH Platform. A dual-output, 80-MHz femtosecond pulsed laser (InSight ×3; Spectra-Physics) provides the pump beam (tunable from 680 to 1,300 nm) and the Stokes beam (fixed at 1,045 nm) for the SRS system (Fig. 1*B*). Stimulated Raman loss provides the SRS intensity by detecting the modulation transfer from the Stokes to the pump beam. The Stokes beam was modulated by an acousto-optic modulator (1205c; Isomet Corporation) at ∼2.26 MHz. The two beams were then combined by the dichroic mirror and directed into a laboratory-built laser scanning microscope. A 60× water objective (UPlanApo 60XW, numerical aperture (NA) = 1.2; Olympus) focused the collinear beams on the sample. The power on the sample was ∼6 mW for the pump beam and ∼32 mW for the Stokes beam. The two-dimensional galvo scanning unit (6215H; Cambridge Technique) was conjugated to the back aperture by a four-focal/telescope with finite conjugates system and scanned the laser focus to create the SRS image. An oil condenser (NA = 1.4, Aplanat Achromat 1.4; Olympus) alleviated the cross-phase modulation-induced background in SRS by better collecting laser beams. The collected beams were filtered by two filters (HA825/150m; Chroma), and only the pump beam was detected by the silicon photodiode (S3994-01; Hamamatsu). Then, the photon-converted electric signal was first separated into alternating current (AC) readout and direct current (DC) readout. Then, the AC signal was amplified by the laboratory-build resonant amplifier circuit centered at ∼2.26 MHz. After that, the AC signal was further extracted by a lock-in amplifier (HF2LI; Zurich Instrument). As the femtosecond pulsed lasers have rather broad bandwidths, femtosecond SRS has a total covering range of 200 cm^{-1} around the peak (29). Thus, in this study, the C-D and C-H signature peaks at 2,040 to 2,300 cm^{-1} and at 2,800 to 3,100 cm^{-1} can be mostly covered by femtosecond SRS.

To incorporate FISH visualization into the platform, we implemented TPEF in the SRS system (Fig. 1 *A*, *Right*). Forward detection with a higher collection efficiency of the condenser better preserved the fluorescence signal. With a flip mirror, the light was directed into the fluorescence collection devices. Two silicon photomultiplier (C14455-3050GA; Hamamatsu) modules were implemented to provide better-quality fluorescence images compared with photomultiplier tubes (H7422-40; Hamamatsu) with an external preamplifier (29). A 75-mm-focal-length lens focused the emission light onto the silicon photomultipliers (SiPMs) with a 605-nm cut-on dichroic mirror (DMLP605; Thorlabs) that separated the emission into two paths. Two filters centered at 570 nm (ET570/20x; Chroma) and 670 nm (ET670/50m; Chroma) were used to detect the fluorescence from different FISH-labeled cells with Cy3 or Cy5, which can be efficiently excited by the Stokes beam and the pump beam (for C-D, C-H, or off resonance due to the wide two-photon absorption bandwidth) in SRS, respectively. A data acquisition card (PCIe-6363; National Instruments) collected the final output to construct the images.

Image Acquisition. Fixed cells were spotted onto a poly-L-lysine–coated coverslip, covered, and sealed by another coverslip with a spacer in between (39). Samples were prepared in this way to reduce cross-phase modulation signal while keeping the sample in the liquid environment that matches the refractive index of the water objective used for imaging. For imaging in the dry conditions, fixed cells were spotted onto a poly-L-lysine–coated coverslip, dried, and then covered by another coverslip with spacers at two opposite sides. For each sample, three FOVs were scanned by a motorized stage or manually for SRS-FISH analysis. Three channels of SRS images (C-D, C-H, and off resonance) and two fluorescence images (Cy3 and Cy5) were collected as a full image set for analyzing two populations targeted with FISH. Although fluorescence images could be acquired simultaneously with stimulated Raman scattering-carbon-deuterium bond by splitting the output beam in the forward direction or collecting epifluorescence signal, limitations in the data acquisition card do not provide higher sampling speed for multichannel sampling. So, all the images were acquired sequentially. Each FOV was 42.82 or 85.62 μm^2 with 214 nm per step and covered around ∼300 to 400 cells or ∼1,200 to 1,600 cells. Depending on the signal intensity level, 10-μs pixel dwell time with ∼1 to 10 frames average was applied for either SRS or fluorescence images. The laser wavelength tuning and stabilizing time for changing between different SRS frames was around 10 s. The throughput of SRS-FISH analysis is around 10 to 100 ms per cell (∼10 to 100 cells per second) by taking into account the FOV moving time and laser wavelength switching time. For the microbiome test of three individuals' samples in eight different conditions, three randomly selected FOVs were measured, which totally covered around 30,000 cells.

Image Processing. After all images were acquired as described in the last section (*SI Appendix*, Fig. S4, step 1), the illumination correction was applied to alleviate the uneven illumination causing intensity variation (*SI Appendix*, Fig. S4, step 2). Subsequently, SRS images were subtracted by the mean background intensity to eliminate the signal from the glass substrate (*SI Appendix*, Fig. S4, step 3). Three channels were rescaled according to the DC readout from the photodiode connected to the resonant amplifier circuit (*SI Appendix*, Fig. S4, step 4). The AC and DC signals were linear to the pump power within the power range used in this experiment. After that, the signal intensities from the off-resonance channels were subtracted from the rescaled C-D and C-H intensities, which eliminated the other pump probe background (*SI Appendix*, Fig. S4, step 5). Then, the $\%CD_{SRS}$ images were calculated (*SI Appendix*, Fig. S4, step 6). Owing to the not perfect pixel by pixel off-resonance subtraction, resulting in overcorrection, and the dominance of I_{off} at low C-D signal intensities, some bacteria with low D content exhibited negative $\%CD_{SRS}$ values (*SI Appendix*, *SI Text*). Fluorescence images acquired in the dry conditions were aligned to SRS images acquired after water immersion to reduce the mask measurement error from sample drift caused by water immersion (*SI Appendix*, Fig. S4, step 7). C-H channels or fluorescence channels were used to generate the single-cell measuring masks depending on the need and availability of the fluorescence images (*SI Appendix*, Fig. S4, steps 8 and 9). The created masks enabled the measurement of single-cell average $\%CD_{SRS}$ values of masked cells (*SI Appendix*, Fig. S4, step 10). By calculating the ratio between the number of bacteria in each FISH channel and in C-H channel, we quantified the percentage of FISH-stained cells per labeling condition for each probe under different sugar amendment conditions (Fig. 4 *F* and *G*). All imaging and statistical analyses were performed with CellProfiler and MATLAB (The MathWorks).

FISH. Fixed cells (100 μL) were pelleted at 14,000 × *g* for 10 min, resuspended in 100 μL 96% analytical grade ethanol, and incubated for 1 min at room temperature for dehydration. Subsequently, the samples were centrifuged at 14,000 × *g* for 5 min, the ethanol was removed, and the cell pellet was air-dried. Cells were hybridized in solution (100 μL) for 3 h at 46 °C. The hybridization buffer consisted of 900 mM NaCl, 20 mM Tris-(hydroxymethyl)-amino methane HCl, 1 mM ethylenediamine tetraacetic acid, and 0.01% sodium dodecyl

sulphate and contained 100 ng of the respective fluorescently labeled oligonucleotide as well as the required formamide concentration to obtain stringent conditions (*SI Appendix*, Table S1). After hybridization, samples were immediately transferred into a centrifuge with a rotor preheated at 46 °C and centrifuged at 14,000 × *g* for 15 min at the maximum allowed temperature (40 °C) to minimize unspecific probe binding. Samples were washed in a buffer of appropriate stringency (91) for 15 min at 48 °C, and cells were centrifuged for 15 min at 14,000 × *g* and finally, resuspended in 20 μL of phosphate buffered saline. Cells (5 μL) were spotted on poly-L-lysine–coated cover glasses (no. 1.5H; thickness of 170 ± 5 μm; Paul Marienfeld EN) and allowed to dry overnight at 4 °C protected from light. Excess of salt was removed by dipping the coverslips two times in ice-cold Milli-Q water, and they were allowed to dry at room temperature protected from light.

The growth and labeling of microbial pure cultures, microbiome incubations, and other methods are in *SI Appendix*, *SI Methods*.

Data Availability. The 16S rRNA gene sequences data have been deposited in the National Center for Biotechnology Information (NCBI) Sequence Read Archive (accession no. PRJNA802995). CellProfiler pipelines and Matlab codes have been deposited in GitHub (https://github.com/buchenglab/srs-fish). All other data are included in the article and/or *SI Appendix*.

ACKNOWLEDGMENTS. Research reported in this publication was funded by NIH Awards R35GM136223 (to J.-X.C.) and R01AI141439 (to J.-X.C.) and supported by the Boston University Micro and Nano Imaging Facility and Office of the Director, NIH Award S10OD024993. Funding for the presented research was also provided via Young Independent Research Group Grant ZK-57 (to F.C.P.) and by Austrian Science Fund Wittgensteinaward Z383-B (to M.W.). The content is solely the responsibility of the authors and does not necessarily represent the official views of the NIH. We thank Jasmin Schwarz, Gudrun Kohl, and Petra Pjevac from the Joint Microbiome Facility of the Medical University of Vienna and the University of Vienna for assisting with amplicon sequencing.

Author affiliations: [a]Department of Electrical & Computer Engineering, Boston University, Boston, MA 02215; [b]Centre for Microbiology and Environmental Systems Science, Department of Microbiology and Ecosystem Science, University of Vienna, 1030 Vienna, Austria; [c]Joint Microbiome Facility of the Medical University of Vienna and the University of Vienna, 1030 Vienna, Austria; [d]Department of Laboratory Medicine, Medical University of Vienna, 1090 Vienna, Austria; [e]Department of Biomedical Engineering, Photonics Center, Boston University, Boston, MA 02215; and [f]Department of Chemistry and Bioscience, Aalborg University, 9220 Aalborg, Denmark

Author contributions: X.G., F.C.P., D.B., M.W., and J.-X.C. designed research; X.G., F.C.P., and M.M. performed research; X.G. and M.Z. contributed new reagents/analytic tools; X.G., F.C.P., M.M., B.H., and J.Z. analyzed data; and X.G., F.C.P., A.S., M.W., and J.-X.C. wrote the paper.

1. J. G. Camp, R. Platt, B. Treutlein, Mapping human cell phenotypes to genotypes with single-cell genomics. *Science* **365**, 1401–1405 (2019).
2. R. Zenobi, Single-cell metabolomics: Analytical and biological perspectives. *Science* **342**, 1243259 (2013).
3. T. M. J. Evers *et al.*, Deciphering metabolic heterogeneity by single-cell analysis. *Anal. Chem.* **91**, 13314–13323 (2019).
4. N. Musat, R. Foster, T. Vagner, B. Adam, M. M. M. Kuypers, Detecting metabolic activities in single cells, with emphasis on nanoSIMS. *FEMS Microbiol. Rev.* **36**, 486–511 (2012).
5. D. Berry *et al.*, Host-compound foraging by intestinal microbiota revealed by single-cell stable isotope probing. *Proc. Natl. Acad. Sci. U.S.A.* **110**, 4720–4725 (2013).
6. S. Scheller, H. Yu, G. L. Chadwick, S. E. McGlynn, V. J. Orphan, Artificial electron acceptors decouple archaeal methane oxidation from sulfate reduction. *Science* **351**, 703–707 (2016).
7. A. T. Reese *et al.*, Microbial nitrogen limitation in the mammalian large intestine. *Nat. Microbiol.* **3**, 1441–1450 (2018).
8. N. Lee *et al.*, Combination of fluorescent in situ hybridization and microautoradiography-a new tool for structure-function analyses in microbial ecology. *Appl. Environ. Microbiol.* **65**, 1289–1297 (1999).
9. M. Nierychlo *et al.*, The morphology and metabolic potential of the Chloroflexi in full-scale activated sludge wastewater treatment plants. *FEMS Microbiol. Ecol.*, 10.1093/femsec/fiy228 (2019).
10. D. Berry *et al.*, Tracking heavy water (D2O) incorporation for identifying and sorting active microbial cells. *Proc. Natl. Acad. Sci. U.S.A.* **112**, E194–E203 (2015).
11. M. Taubert *et al.*, Tracking active groundwater microbes with D_2 O labelling to understand their ecosystem function. *Environ. Microbiol.* **20**, 369–384 (2018).
12. W. E. Huang *et al.*, Resolving genetic functions within microbial populations: In situ analyses using rRNA and mRNA stable isotope probing coupled with single-cell Raman-fluorescence in situ hybridization. *Appl. Environ. Microbiol.* **75**, 234–241 (2009).
13. G. J. Olsen, D. J. Lane, S. J. Giovannoni, N. R. Pace, D. A. Stahl, Microbial ecology and evolution: A ribosomal RNA approach. *Annu. Rev. Microbiol.* **40**, 337–365 (1986).
14. K. S. Lee *et al.*, An automated Raman-based platform for the sorting of live cells by functional properties. *Nat. Microbiol.* **4**, 1035–1048 (2019).
15. T. Fang, W. Shang, C. Liu, Y. Liu, A. Ye, Single-cell multimodal analytical approach by integrating raman optical tweezers and RNA sequencing. *Anal. Chem.* **92**, 10433–10441 (2020).
16. Y. Wang *et al.*, Raman activated cell ejection for isolation of single cells. *Anal. Chem.* **85**, 10697–10701 (2013).
17. F. C. Pereira *et al.*, Rational design of a microbial consortium of mucosal sugar utilizers reduces *Clostridiodes difficile* colonization. *Nat. Commun.* **11**, 5104 (2020).
18. A. Zumbusch, G. R. Holtom, X. S. Xie, Three-dimensional vibrational imaging by coherent anti-Stokes Raman scattering. *Phys. Rev. Lett.* **82**, 4142–4145 (1999).
19. J. X. Cheng, W. Min, Y. Ozeki, D. Polli, *Stimulated Raman Scattering Microscopy: Techniques and Applications* (Elsevier, 2021).
20. W. Min, C. W. Freudiger, S. Lu, X. S. Xie, Coherent nonlinear optical imaging: Beyond fluorescence microscopy. *Annu. Rev. Phys. Chem.* **62**, 507–530 (2011).
21. D. Fu *et al.*, Quantitative chemical imaging with multiplex stimulated Raman scattering microscopy. *J. Am. Chem. Soc.* **134**, 3623–3626 (2012).
22. M. Ji *et al.*, Detection of human brain tumor infiltration with quantitative stimulated Raman scattering microscopy. *Sci. Transl. Med.* **7**, 309ra163 (2015).
23. S. Yue, J. X. Cheng, Deciphering single cell metabolism by coherent Raman scattering microscopy. *Curr. Opin. Chem. Biol.* **33**, 46–57 (2016).
24. A. Zumbusch, W. Langbein, P. Borri, Nonlinear vibrational microscopy applied to lipid biology. *Prog. Lipid Res.* **52**, 615–632 (2013).
25. L. Shi *et al.*, Optical imaging of metabolic dynamics in animals. *Nat. Commun.* **9**, 2995 (2018).
26. Y. Wakisaka *et al.*, Probing the metabolic heterogeneity of live *Euglena gracilis* with stimulated Raman scattering microscopy. *Nat. Microbiol.* **1**, 16124 (2016).
27. S. Yue *et al.*, Cholesteryl ester accumulation induced by PTEN loss and PI3K/AKT activation underlies human prostate cancer aggressiveness. *Cell Metab.* **19**, 393–406 (2014).
28. J. Li *et al.*, Abrogating cholesterol esterification suppresses growth and metastasis of pancreatic cancer. *Oncogene* **35**, 6378–6388 (2016).
29. K. C. Huang, J. Li, C. Zhang, Y. Tan, J. X. Cheng, Multiplex stimulated Raman scattering imaging cytometry reveals lipid-rich protrusions in cancer cells under stress condition. *iScience* **23**, 100953 (2020).
30. J. Li *et al.*, Lipid desaturation is a metabolic marker and therapeutic target of ovarian cancer stem cells. *Cell Stem Cell* **20**, 303–314.e5 (2017).
31. H. J. Lee *et al.*, Multimodal metabolic imaging reveals pigment reduction and lipid accumulation in metastatic melanoma. *BME Front.* **2021**, 9860123 (2021).
32. J. Du *et al.*, Raman-guided subcellular pharmaco-metabolomics for metastatic melanoma cells. *Nat. Commun.* **11**, 4830 (2020).
33. T. Hellerer *et al.*, Monitoring of lipid storage in *Caenorhabditis elegans* using coherent anti-Stokes Raman scattering (CARS) microscopy. *Proc. Natl. Acad. Sci. U.S.A.* **104**, 14658–14663 (2007).
34. M. C. Wang, W. Min, C. W. Freudiger, G. Ruvkun, X. S. Xie, RNAi screening for fat regulatory genes with SRS microscopy. *Nat. Methods* **8**, 135–138 (2011).
35. W. W. Chen *et al.*, Spectroscopic coherent Raman imaging of Caenorhabditis elegans reveals lipid particle diversity. *Nat. Chem. Biol.* **16**, 1087–1095 (2020).
36. A. S. Mutlu, S. M. Gao, H. Zhang, M. C. Wang, Olfactory specificity regulates lipid metabolism through neuroendocrine signaling in *Caenorhabditis elegans*. *Nat. Commun.* **11**, 1450 (2020).
37. J. Li, J. X. Cheng, Direct visualization of de novo lipogenesis in single living cells. *Sci. Rep.* **4**, 6807 (2014).
38. L. Zhang *et al.*, Spectral tracing of deuterium for imaging glucose metabolism. *Nat. Biomed. Eng.* **3**, 402–413 (2019).
39. M. Zhang *et al.*, Rapid determination of antimicrobial susceptibility by stimulated raman scattering imaging of D_2O metabolic incorporation in a single bacterium. *Adv. Sci.* **7**, 2001452 (2020).
40. J. M. Levsky, R. H. Singer, Fluorescence in situ hybridization: Past, present and future. *J. Cell Sci.* **116**, 2833–2838 (2003).
41. W. E. Huang *et al.*, Raman-FISH: Combining stable-isotope Raman spectroscopy and fluorescence in situ hybridization for the single cell analysis of identity and function. *Environ. Microbiol.* **9**, 1878–1889 (2007).
42. E. Y. Fernando *et al.*, Resolving the individual contribution of key microbial populations to enhanced biological phosphorus removal with Raman-FISH. *ISME J.* **13**, 1933–1946 (2019).
43. R. Sender, S. Fuchs, R. Milo, Revised estimates for the number of human and bacteria cells in the body. *PLoS Biol.* **14**, e1002533 (2016).
44. J. A. Gilbert *et al.*, Current understanding of the human microbiome. *Nat. Med.* **24**, 392–400 (2018).
45. D. Valentine, A. Sessions, S. Tyler, A. Chidthaisong, Hydrogen isotope fractionation during H_2/CO_2 acetogenesis: Hydrogen utilization efficiency and the origin of lipid-bound hydrogen. *Geobiology* **2**, 179–188 (2004).
46. R. Starke *et al.*, Tracing incorporation of heavy water into proteins for species-specific metabolic activity in complex communities. *J. Proteomics* **222**, 103791 (2020).
47. Y. Wang *et al.*, Raman-deuterium isotope probing to study metabolic activities of single bacterial cells in human intestinal microbiota. *Microb. Biotechnol.* **13**, 572–583 (2020).
48. D. Zhang, M. N. Slipchenko, J. X. Cheng, Highly sensitive vibrational imaging by femtosecond pulse stimulated Raman loss. *J. Phys. Chem. Lett.* **2**, 1248–1253 (2011).
49. M. A. Albota, C. Xu, W. W. Webb, Two-photon fluorescence excitation cross sections of biomolecular probes from 690 to 960 nm. *Appl. Opt.* **37**, 7352–7356 (1998).
50. D. Zhang, M. N. Slipchenko, D. E. Leaird, A. M. Weiner, J. X. Cheng, Spectrally modulated stimulated Raman scattering imaging with an angle-to-wavelength pulse shaper. *Opt. Express* **21**, 13864–13874 (2013).
51. P. Berto, E. R. Andresen, H. Rigneault, Background-free stimulated Raman spectroscopy and microscopy. *Phys. Rev. Lett.* **112**, 053905 (2014).
52. G. A. Matanfack *et al.*, Influence of carbon sources on quantification of deuterium incorporation in heterotrophic bacteria: A Raman-stable isotope labeling approach. *Anal. Chem.* **92**, 11429–11437 (2020).
53. W. Manz, R. Amann, W. Ludwig, M. Vancanneyt, K. H. Schleifer, Application of a suite of 16S rRNA-specific oligonucleotide probes designed to investigate bacteria of the phylum cytophaga-flavobacter-bacteroides in the natural environment. *Microbiology (Reading)* **142**, 1097–1106 (1996).

54. W. Manz, R. Amann, W. Ludwig, M. Wagner, K. H. Schleifer, Phylogenetic oligodeoxynucleotide probes for the major subclasses of proteobacteria: Problems and solutions. *Syst. Appl. Microbiol.* **15**, 593–600 (1992).
55. J. X. Cheng, X. S. Xie, *Coherent Raman Scattering Microscopy* (CRC Press, 2016).
56. L. E. Tailford, E. H. Crost, D. Kavanaugh, N. Juge, Mucin glycan foraging in the human gut microbiome. *Front. Genet.* **6**, 81 (2015).
57. F. C. Pereira, D. Berry, Microbial nutrient niches in the gut. *Environ. Microbiol.* **19**, 1366–1378 (2017).
58. J. M. H. Larsson, H. Karlsson, H. Sjövall, G. C. Hansson, A complex, but uniform O-glycosylation of the human MUC2 mucin from colonic biopsies analyzed by nanoLC/MSn. *Glycobiology* **19**, 756–766 (2009).
59. K. A. Thomsson *et al.*, Detailed O-glycomics of the Muc2 mucin from colon of wild-type, core 1- and core 3-transferase-deficient mice highlights differences compared with human MUC2. *Glycobiology* **22**, 1128–1139 (2012).
60. L. Rigottier-Gois, V. Rochet, N. Garrec, A. Suau, J. Doré, Enumeration of Bacteroides species in human faeces by fluorescent in situ hybridisation combined with flow cytometry using 16S rRNA probes. *Syst. Appl. Microbiol.* **26**, 110–118 (2003).
61. S. Mueller *et al.*, Differences in fecal microbiota in different European study populations in relation to age, gender, and country: A cross-sectional study. *Appl. Environ. Microbiol.* **72**, 1027–1033 (2006).
62. A. H. Franks *et al.*, Variations of bacterial populations in human feces measured by fluorescent in situ hybridization with group-specific 16S rRNA-targeted oligonucleotide probes. *Appl. Environ. Microbiol.* **64**, 3336–3345 (1998).
63. D. A. Ravcheev, I. Thiele, Comparative genomic analysis of the human gut microbiome reveals a broad distribution of metabolic pathways for the degradation of host-synthetized mucin glycans and utilization of mucin-derived monosaccharides. *Front. Genet.* **8**, 111 (2017).
64. E. Fadeev *et al.*, Comparison of two 16s rrna primers (v3–v4 and v4–v5) for studies of arctic microbial communities. *Front. Microbiol.* **12**, 637526 (2021).
65. I. Bakenhus *et al.*, Distinct relationships between fluorescence in situ hybridization and 16S rRNA gene- and amplicon-based sequencing data of bacterioplankton lineages. *Syst. Appl. Microbiol.* **42**, 126000 (2019).
66. N. Zmora, D. Zeevi, T. Korem, E. Segal, E. Elinav, Taking it personally: Personalized utilization of the human microbiome in health and disease. *Cell Host Microbe* **19**, 12–20 (2016).
67. C. F. Maurice, H. J. Haiser, P. J. Turnbaugh, Xenobiotics shape the physiology and gene expression of the active human gut microbiome. *Cell* **152**, 39–50 (2013).
68. B. T. Hanson *et al.*, Sulfoquinovose is a select nutrient of prominent bacteria and a source of hydrogen sulfide in the human gut. *ISME J.* **15**, 2779–2791 (2021).
69. L. Hoskins, E. Boulding, T. Gerken, V. Harouny, M. Kriaris, Mucin glycoprotein degradation by mucin oligosaccharide-degrading strains of human faecal bacteria. Characterisation of saccharide cleavage products and their potential role in nutritional support of larger faecal bacterial populations. *Microb. Ecol. Health Dis.* **5**, 193–207 (1992).
70. P. Van den Abbeele *et al.*, Butyrate-producing Clostridium cluster XIVa species specifically colonize mucins in an in vitro gut model. *ISME J.* **7**, 949–961 (2013).
71. A. Lombardini *et al.*, Background-suppressed SRS fingerprint imaging with a fully integrated system using a single optical parametric oscillator. *Opt. Express* **28**, 14490–14502 (2020).
72. M. Nierychlo, J. L. Nielsen, P. H. Nielsen, "Studies of the ecophysiology of single cells in microbial communities by (quantitative) microautoradiography and fluorescence in situ hybridization (MAR-FISH)" in *Hydrocarbon and Lipid Microbiology Protocols: Ultrastructure and Imaging*, T. J. McGenity, K. N. Timmis, B. Nogales, Eds. (Springer Protocols Handbooks, Springer, Berlin, Germany, 2016), pp. 115–130.
73. N. R. Meyer, J. L. Fortney, A. E. Dekas, NanoSIMS sample preparation decreases isotope enrichment: Magnitude, variability and implications for single-cell rates of microbial activity. *Environ. Microbiol.* **23**, 81–98 (2021).
74. M. S. Desai *et al.*, A dietary fiber-deprived gut microbiota degrades the colonic mucus barrier and enhances pathogen susceptibility. *Cell* **167**, 1339–1353.e21 (2016).
75. J. M. Pickard, A. V. Chervonsky, Intestinal fucose as a mediator of host-microbe symbiosis. *J. Immunol.* **194**, 5588–5593 (2015).
76. R. J. Kelly, S. Rouquier, D. Giorgi, G. G. Lennon, J. B. Lowe, Sequence and expression of a candidate for the human secretor blood group α(1,2)Fucosyltransferase Gene (FUT2): Homozygosity for an enzyme-inactivating nonsense mutation commonly correlates with the non-secretor phenotype. *J. Biol. Chem.* **270**, 4640–4649 (1995).
77. P. Rausch *et al.*, Colonic mucosa-associated microbiota is influenced by an interaction of Crohn disease and FUT2 (Secretor) genotype. *Proc. Natl. Acad. Sci. U.S.A.* **108**, 19030–19035 (2011).
78. P. C. Kashyap *et al.*, Genetically dictated change in host mucus carbohydrate landscape exerts a diet-dependent effect on the gut microbiota. *Proc. Natl. Acad. Sci. U.S.A.* **110**, 17059–17064 (2013).
79. M. Brinkmann *et al.*, Portable all-fiber dual-output widely tunable light source for coherent Raman imaging. *Biomed. Opt. Express* **10**, 4437–4449 (2019).
80. Y. Bi *et al.*, Near-resonance enhanced label-free stimulated Raman scattering microscopy with spatial resolution near 130 nm. *Light Sci. Appl.* **7**, 81 (2018).
81. M. Zhuge *et al.*, Ultrasensitive vibrational imaging of retinoids by visible preresonance stimulated raman scattering microscopy. *Adv. Sci. (Weinh.)* **8**, 2003136 (2021).
82. A. M. Valm, J. L. Mark Welch, G. G. Borisy, CLASI-FISH: Principles of combinatorial labeling and spectral imaging. *Syst. Appl. Microbiol.* **35**, 496–502 (2012).
83. M. Lukumbuzya, M. Schmid, P. Pjevac, H. Daims, A multicolor fluorescence *in situ* hybridization approach using an extended set of fluorophores to visualize microorganisms. *Front. Microbiol.* **10**, 1383 (2019).
84. H. Shi *et al.*, Highly multiplexed spatial mapping of microbial communities. *Nature* **588**, 676–681 (2020).
85. H. Lin *et al.*, Microsecond fingerprint stimulated Raman spectroscopic imaging by ultrafast tuning and spatial-spectral learning. *Nat. Commun.* **12**, 3052 (2021).
86. H. R. Gruber-Vodicka *et al.*, Paracatenula, an ancient symbiosis between thiotrophic Alphaproteobacteria and catenulid flatworms. *Proc. Natl. Acad. Sci. U.S.A.* **108**, 12078–12083 (2011).
87. N. Majed, T. Chernenko, M. Diem, A. Z. Gu, Identification of functionally relevant populations in enhanced biological phosphorus removal processes based on intracellular polymers profiles and insights into the metabolic diversity and heterogeneity. *Environ. Sci. Technol.* **46**, 5010–5017 (2012).
88. L. Wei *et al.*, Imaging complex protein metabolism in live organisms by stimulated Raman scattering microscopy with isotope labeling. *ACS Chem. Biol.* **10**, 901–908 (2015).
89. H. J. Lee, J. X. Cheng, Imaging chemistry inside living cells by stimulated Raman scattering microscopy. *Methods* **128**, 119–128 (2017).
90. C. W. Freudiger *et al.*, Label-free biomedical imaging with high sensitivity by stimulated Raman scattering microscopy. *Science* **322**, 1857–1861 (2008).
91. H. Daims, "The family Nitrospiraceae" in *The Prokaryotes: Other Major Lineages of Bacteria and the Archaea*, E. Rosenberg, E. F. DeLong, S. Lory, E. Stackebrandt, F. Thompson, Eds. (Springer, Berlin, Germany, 2014), pp. 733–749.